Structural and optical properties of hematite and L-arginine/hematite nanostructures prepared by thermal spray pyrolysis

Justine Sageka Nyarige, Tjaart P. J. Krüger, Mmantsae Diale

Department of Physics, University of Pretoria, Private Bag X20, Hatfield, 0028, South Africa,

Corresponding author email address: mmantsae.diale@up.ac.za

Abstract

A study of structural and optical properties of hematite and L-arginine/hematite films was carried out. Hematite films were deposited by thermal spray pyrolysis on fluorine-doped tin oxide at temperatures varying from 280 to 430°C. X-ray diffraction results revealed (104) and (110) planes, describing the rhombohedral structure of hematite. Scanning electron microscopy on hematite films showed nanoparticles of grain sizes ranging between 40 and 100±0.5 nm. Hematite nanoparticles were transformed to nanospheres with uniform size of 35±0.5 nm, using chemical bath deposition and L-arginine as the biomolecule. Raman peaks revealed two A_{1g} and five E_g phonon vibrational modes of hematite. Atomic force microscopy confirmed an increase of surface root mean square roughness from 35 to 40 nm for hematite nanoparticles and L-arginine/hematite respectively which is desirable for charge transport. The films exhibited an indirect band gap varying from 2.08 to 2.30 eV and onset absorbance that ranged between 525 and 560 nm.

Key-words: Spray pyrolysis, chemical bath deposition, hematite, L-arginine, nanostructures

1. Introduction

Global energy consumption has been rising due to an increase in world population and industrialization [1]. Solar is the most abundant, environmentally friendly energy source in mitigating global energy problem. It can be transformed into electrical energy then stored as fuel in form of hydrogen through electrolysis of water [2]. Photoelectrochemical (PEC) water splitting is one of the approaches that employ the use of semiconductors to split water and store solar energy as a hydrogen fuel [3]. Since the initial report of low-efficiency hydrogen production by Fujishima and Honda on PEC water splitting using titanium dioxide (TiO_2) [4], a number of other materials have been explored for. These materials include cadmium selenide (CdSe), zinc oxide (ZnO), copper (1) oxide (Cu_2O), tungsten trioxide (WO_3) and hematite (α-Fe_2O_3) [4-9]. However, the band edge alignments of these semiconductors do not straddle water oxidation and reduction potentials. Of these materials, hematite, an n-type semiconductor, has received much attention for PEC water splitting due to its stability in aqueous medium, a small indirect band gap of 1.90 eV-2.20 eV, non-toxicity and abundance [10, 11]. However, there are associated limitations such as high electron-hole recombination rate, short hole diffusion length (2- 4 nm) with short excited lifetime of 10 ps, poor minority charge carrier of 0.1 $cm^2\ V^{-1}s^{-1}$, leading to low photocurrent production during water splitting [12]. Hematite promises maximum theoretical solar to hydrogen (STH) efficiency of ~16.8 %, with photocurrent densities above 12 $mAcm^{-2}$, but the reported findings are far below 10 $mAcm^{-2}$ [8,13,14]. Nanostructured photoanodes that decouple light absorption pathway from electrical transport [15] have been reported to mitigate some of these challenges of hematite in water splitting. Hematite nanostructures like nanorods, nanosheets, nanocubes, nanocones, and cauliflowers, synthesized by various methods have been reported [16-19]. The shape and structure of the nanostructures can be altered by biominerals grown on hematite layer. This process has been exploited by integrating biology in nanotechnology to produce thin films with better structural, electrical and optical properties [20] than planar films. The latter has been achieved by different synthesis techniques. Some of the techniques used in synthesis of α-Fe_2O_3 include sol-gel [21], hydrothermal [22], electrodeposition [23], microwave-assisted hydrothermal [24], dip coating [25], SILAR deposition [8], spin-coating [26], microemulsion-precipitation [27] spray pyrolysis [28], among others.

Chemical spray pyrolysis (CSP) is one of the simplest deposition techniques used in the synthesis of thin films. CSP consists of a solution container, substrate heater, temperature controller and an atomizer[29]. Micro-droplets of the precursor solution dissolved in a less volatile solution are generated by the atomizer. The droplets are then transported by a carrier gas, which is normally an inert, out of the nozzle to the pre-heated substrate where the spraying takes place. For a complete decomposition and formation of good quality films, optimum substrate temperature is required. This enables the evaporation of volatile solvents used in the preparation of the precursor solution. Chemical bath deposition (CBD) has also been used in the preparation of thin films that can provide a scalable approach in the transformation of hematite nanostructures [30]. The films prepared by the two methods can be used for photovoltaic applications, water splitting and may improve the efficiency of hydrogen gas production.

Research has shown that crystal shapes of biomineral structure are different from those grown using a pure precursor solution hence the motivation of our study to incorporate a biomolecule on planar hematite structure using chemical bath deposition. In

this study, α-Fe_2O_3 nanostructures were prepared using chemical spray pyrolysis at temperatures of 280°C, 330°C, 380°C, and 430°C. L-arginine, an amino acid with α-amino group and α-carboxylic acid group as the components was used in the transformation of the architecture of the nanostructures. Hematite nanoparticles (NPs) that have no definite shape were transformed to nanospheres with uniform shape using L-arginine through chemical bath deposition. The reaction involved equimolar solutions of $FeCl_3.6H_2O$ and L-arginine with deionized water as a solvent. The films synthesized by L-arginine had better morphological, structural and optical properties as opposed to planar hematite ones and have an application for PEC water splitting to produce hydrogen gas.

2. Experimental section

2.1 Substrate cleaning

Soda lime glass and fluorine-doped tin oxide (FTO) substrates were cleaned by first soaking in a solution of sodium hydroxide (NaOH) and 0.5 M sodium stearate ($C_{17}H_{35}COONa$) for 10 minutes, followed by rinsing with deionised water. The rinsed substrates were placed in ethanol and agitated in an ultrasonic bath for 10 minutes, rinsed again with deionised water, and agitated in acetone using the same conditions. They were finally rinsed with deionised water and blown dry with nitrogen gas.

2.2 Synthesis of hematite nanostructures

Hematite films were deposited using the CSP method. 50 mM of $Fe(NO_3)_3.9H_2O$ (Sigma Aldrich, AR, 99.99%) was dissolved in 200 ml of deionized water and stirred to obtain a homogeneous solution. The homogeneous solution was then sprayed onto a pre-heated glass substrate using a nozzle of 1 mm diameter. The spraying time was set at 45 seconds. A nozzle to substrate height of 28 cm, molarity of 50 mM and a spray rate of 10 ml/min were used. A resistor thermocouple was used to measure the deposition temperature that was varied from 280°C to 430°C in steps of 50°C, while the flow meter measured the rate. Fig. 1a illustrates the CSP set up used. L-arginine ($C_6H_{14}N_4O_2$) was used to transform hematite NPs with no definite shape to nanospheres using chemical bath deposition as shown in fig. 1b. Equi-molar solutions of $FeCl_3.6H_2O$ and L-arginine were used, with synthesized hematite film at 430°C as the seed layer. Solution A was obtained by dissolving 25 ml of 50 mM of $FeCl_3.6H_2O$ (Sigma Aldrich, AR, 99.99% of pure) in deionized water. 25 ml of L-arginine ($C_6H_{14}N_4O_2$, >99 % pure) was dissolved in deionized water to obtain solution B, that was then added drop-wise to solution A with a lot of stirring to obtain a homogeneous solution. The solution was used to obtain hematite nanospheres at a growth temperature of 90°C, for 48 hours. Prepared films were later rinsed with ethanol and distilled water and left to dry for 12 hours at room temperature before characterization.

2.3 Characterization

X-ray patterns of α-Fe_2O_3 films were identified using German Bruker D2 PHASER X-ray diffraction with CuK_α radiation (1.5418 Å) source, and 2 theta range of 20° to 80°. Raman spectroscopy was measured using WITec alpha300 RAS+ confocal Raman microscope with 532 nm excitation laser. Morphology and thickness of α-Fe_2O_3 films were determined with field emission scanning electron microscope (ZEISS Ultra PLUS FE-SEM-Microscopes). Grain sizes of NPs were determined using imageJ software and Gaussian fitting. Topography of the films was performed by Veeco Nanoman V Atomic Force Microscopy (AFM) technique operated using tapping mode with a scan rate of 2.441 Hz and scan size of 10 µm. Gwydion software was used to determine the roughness of films as observed by AFM for films synthesized by both CSP and CBD. Transmittance, reflectance, and absorbance measurements were carried out using a Cary 100 Bio UV-Vis spectrophotometer.

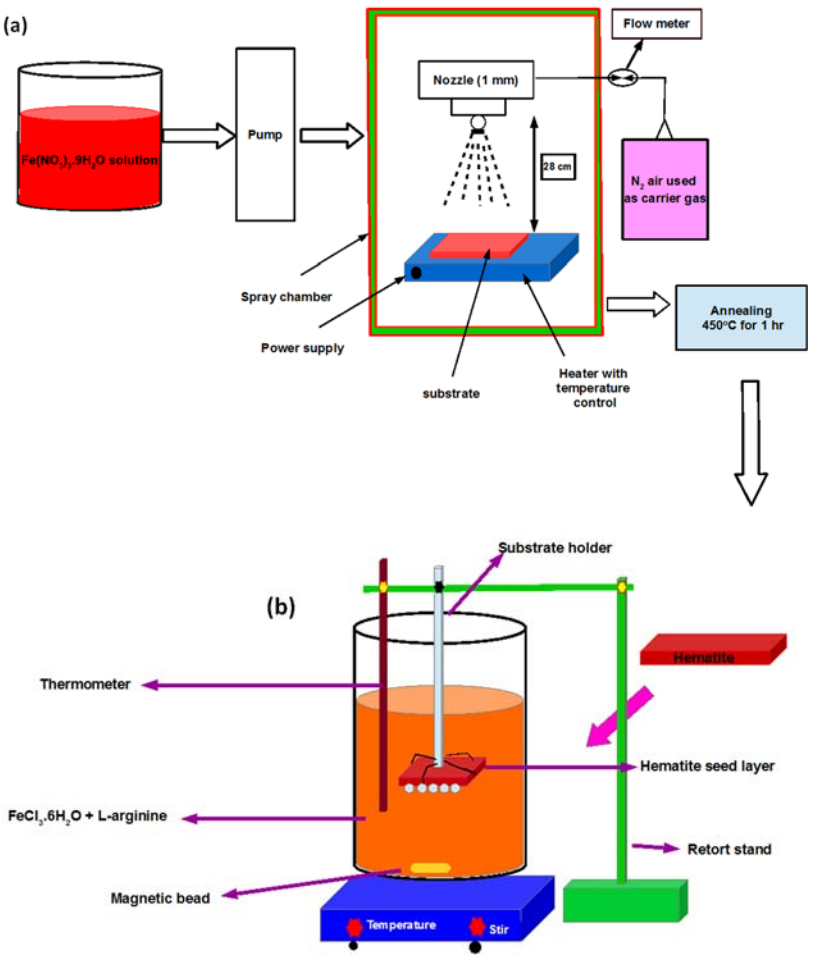

Fig. 1. (a) Setup for spray pyrolysis used to synthesize hematite NPs (b) chemical bath deposition of L-arginine/hematite nanostructures.

3. Results and discussion

Hematite NPs were formed through phase transformation whereby Fe^{3+} was provided by Fe $(NO_3)_3.9H_2O$ and OH^- from water. The reaction formed iron oxyhydrate $(Fe(OH)_3)$, annealed at 450°C for 1 hour to form α-Fe_2O_3 according to equations:

$$Fe(NO_3)_3.9H_2O \rightarrow Fe^{3+} + 3NO_3^- + 9H_2 \quad (1)$$

$$Fe^{3+} + 3(OH)^- \rightarrow Fe(OH)_3 \quad (2)$$

$$2Fe(OH)_3(\text{annealing}) \rightarrow \alpha - Fe_2O_3 \quad (3)$$

Similar formation of hematite has been reported by Yadav's research group [31] using spray pyrolysis with $FeCl_3$ as the precursor.

3.1 X-ray diffraction analysis

The crystal structure of hematite NPs at different deposition temperatures with two theta range of 20° and 80° is shown in fig. 2. All patterns from fig. 2a show the characteristic hematite, matching with the JCPDS plot card no. 84-0311 [31]. XRD planes which represent rhombohedral structure of hematite, space group $R\bar{3}C$, lattice constants a = 0.5034 nm and c = 1.375 nm [27] were indexed at their right two-theta positions. The (012), (104), (110), (113), (024), (116), (122) and (124) peaks corresponded to two-theta angles at 24°, 33°, 35°, 41°, 49°, 54°, 57° and 63° respectively, which are pure phases of hematite structure. XRD revealed sharp hematite peaks, further proving high crystallinity [27, 32]. (104) and (110) were the most intense peaks with a random orientation crystallites for hematite NPs synthesized at different temperatures (280 – 430°C). The two peaks, (104) and (110)

fully describe the rhombohedral structure of hematite and further shows that the growth of the hematite was perpendicular to crystallographic planes [33]. This further shows that synthesized films can have good PEC applications.

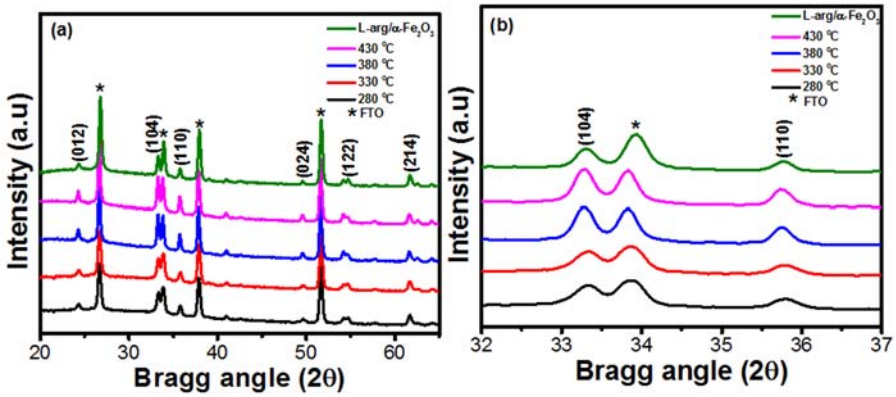

Fig. 2. X-ray diffraction (XRD) pattern of (a) α-Fe_2O_3 films deposited at different temperatures (280-430°C) using chemical spray pyrolysis, (b) (104) and (110) XRD peaks.

The full width at half maximum (FWHM) was calculated using (104) and (110) peaks while Debye Scherer's formula was used to calculate the crystallite size [27],

$$D = \frac{k\lambda}{\beta \cos\theta}, \tag{4}$$

where D is the crystal size, k the shape factor (0.9), λ the wavelength (0.15418 nm, CuK_α), β is full width at half maximum (FWHM) and θ is the diffraction angle of (104) and (110) phases. α-Fe_2O_3 crystallite sizes ranging between 21 nm and 46 nm were obtained, Table 1.

Table 1: FWHM and crystal sizes of hematite NPs prepared by spray pyrolysis at different deposition temperatures and L-arginine/hematite nanospheres synthesized by CBD at a bath temperature of 90°C for 48 hours.

Sample	FWHM (°)	Crystal size of 104 peak (nm)	FWHM (°)	Crystal size of 110 peak (nm)
280°C	0.3238	29.38	0.2370	40.10
330°C	0.3356	28.35	0.2561	38.03
380°C	0.3875	24.54	0.3031	32.14
430°C	0.4473	21.26	0.2736	35.57
L-arg/α-Fe_2O_3	0.3497	27.22	0.2136	45.61

The deposition temperature had an effect on the crystallite size of hematite NPs. At low temperature (280°C), there was formation of large grains, leading to higher crystallite sizes and widening of the peak as opposed to higher deposition temperature (430°C). This was attributed to high evaporation of precursor at high temperature before reaching the substrate which is not the same case at lower temperatures (280°C and 330°C). However, there was an increase in crystallite size for L-arginine/ α-Fe_2O_3 nanospheres. This can be attributed to erosion of planar hematite NPs by L-arginine during the growth process. Therefore, stoichiometry and structure of the particles can be affected by an increase in the crystal size [34].

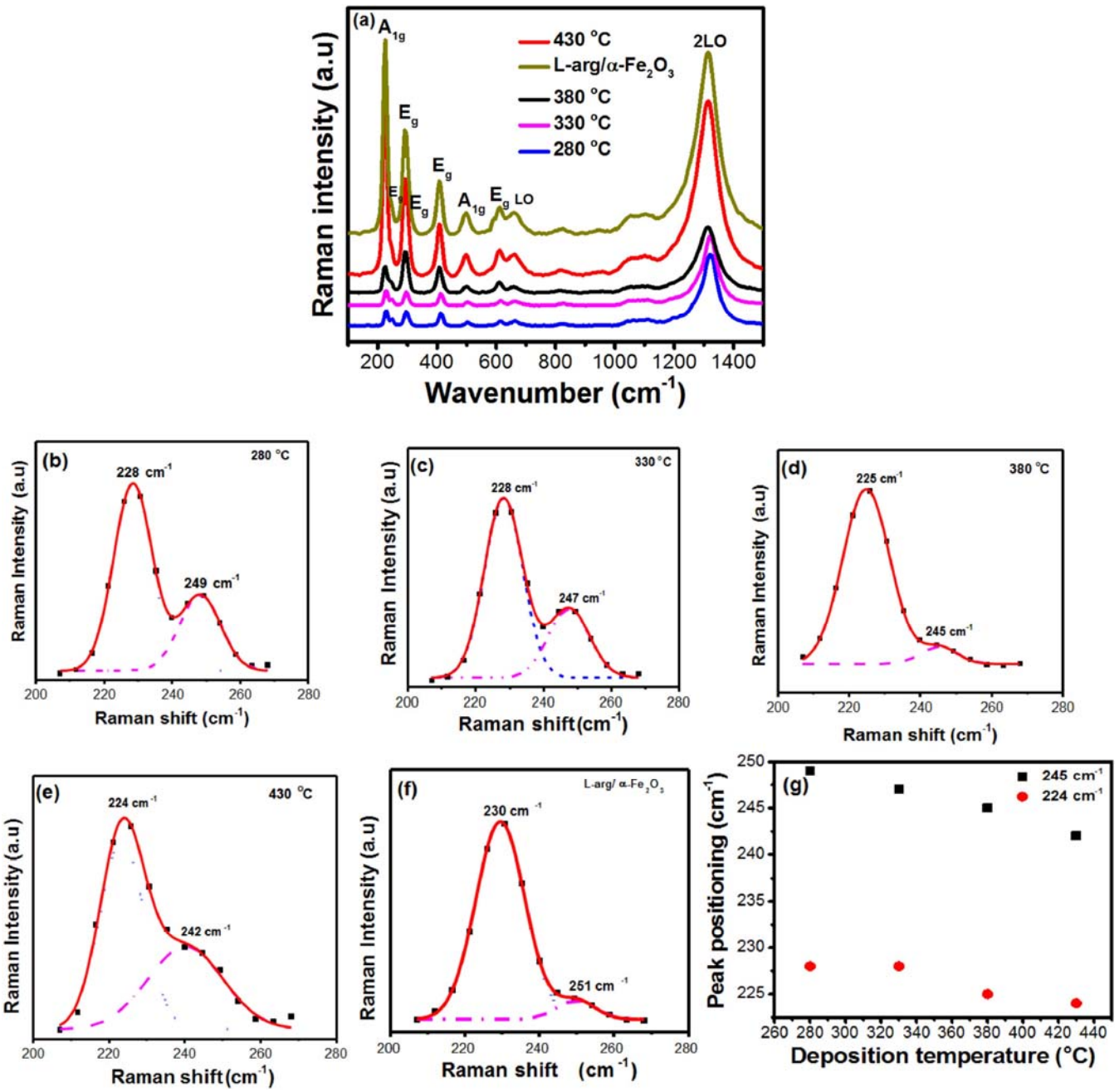

Fig. 3. (a) Raman spectroscopy of α-Fe_2O_3 NPs at deposition temperatures of 280°C, 330°C, 380°C and 430°C using chemical spray pyrolysis, (b-f) Deconvolution of 226 cm^{-1} and 245 cm^{-1} Raman peaks of hematite NPs prepared by spray pyrolysis at a deposition temperature of 280°C, 330°C, 380°C, 430°C and L-arginine/hematite nanospheres prepared by chemical bath deposition at a bath temperature of 90°C for 48 hours, (g) Raman peak positioning of 225 cm^{-1} and 245 cm^{-1} peaks against deposition temperature of α-Fe_2O_3 NPs prepared by spray pyrolysis.

3.2 Raman spectroscopy

Raman peaks of hematite films are represented in Fig. 3. The synthesized hematite nanostructures were all polycrystalline as revealed by sharp and strong Raman vibrational modes at 225 cm^{-1} (A_{1g}), 245 cm^{-1} (E_g), 291 cm^{-1} (E_g), 300 cm^{-1} (E_g) 409 cm^{-1} (E_g), 500 cm^{-1} (A_{1g}) and 609 cm^{-1} (E_g) [4]. The peak at 660 cm^{-1} observed in all samples is associated with the Longitudinal

Optical (LO) mode of hematite, while the 1312 cm^{-1} peak, which is almost double the frequency of the 660 cm^{-1} band, was identified as a two-phonon (magnon) scattering mode (2LO) [5]. The shifting of the peaks with variation of temperature led 2LO mode not to be exactly double wavenumber of LO (660 cm^{-1}) as expected. The intensity of peaks increased for L-arginine/hematite nanospheres as compared to the pristine hematite due to change in crystal size.
Fig. 3 (b-f) shows deconvoluted peaks of 225 cm^{-1} (A_{1g}) and 245 cm^{-1} (E_g) which were not clearly visible in Fig. 3a due to vibrational overlap of A_{1g} and E_g phonon modes. The two vibrational modes of hematite were red-shifted as the deposition temperature increased from 280°C to 430°C. This is attributed to thermal expansion that led to induced transformations in the hematite crystals, hence affecting the population and vibrational energy of different levels of phonon modes [35]. The red shifting of vibrational modes was also influenced by the variation of half-widths (Γ) at different deposition temperatures [36]. 245 cm^{-1} (E_g) peaks were broadening as the temperature increased from 280°C to 430°C. This was due to phonon-phonon scattering caused by the anharmonic terms [36]. The peaks of magnetite or maghemite were not observed, which further revealed the purity of synthesized α-Fe_2O_3 films. The intensity of most of the peaks increased with deposition temperature from 280°C to 430°C. This was due to improvement of crystallinity at higher temperatures. The Raman shift was nonlinear as the temperature was increased gradually from 280°C to 430°C in steps of 50 °C as shown in Fig. 3g.

3.3 Thickness of hematite nanostructures

Field emission scanning electron microscope (FE-SEM) was used to measure thickness of α-Fe_2O_3 thin films using the average cross-section of all samples at different temperatures (280°C to 430°C) as shown with arrows, in Fig. 4a. This excluded thickness of substrate (FTO) and glass that clearly had different layers. There was a decrease in thickness of hematite films as the deposition temperature was increased from 280°C to 430°C in steps of 50°C. Fig. 4b shows the trend of thickness with temperature. At the lowest temperature (280°C), there was high growth rate as most of the precursor was depositing on the FTO substrate making the films thick. This was different at higher temperatures (380°C and 430°C) where high evaporation rate of the $Fe(NO_3)_3.9H_2O$ solution before reaching the substrate. This, therefore, led to deposition of precursor in vapor phase producing transparent films.

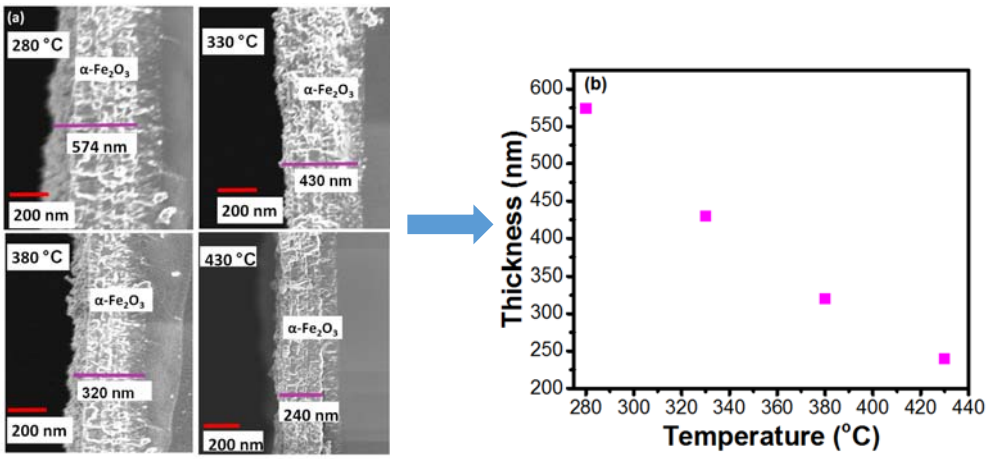

Fig. 4. (a) Cross section micrograph images of hematite (α-Fe_2O_3) obtained using FE-SEM for films deposited at 280°C 330°C 380°C and 430°C using spray pyrolysis. The scale bar of 200 nm (red bar) was used and the thickness of hematite NPs on the substrate was estimated (purple line), (b) a plot of thickness (±0.5 nm) versus temperature for α-Fe_2O_3 thin films at a deposition time of 45 seconds, spray pressure of 1.5 ×10^5 Pa and concentration of 50 mM.

3.4 Surface morphology and topography

3.4.1 Hematite nanostructures

The morphology and topography of hematite thin films prepared at different substrate temperatures are shown in Fig. 5.

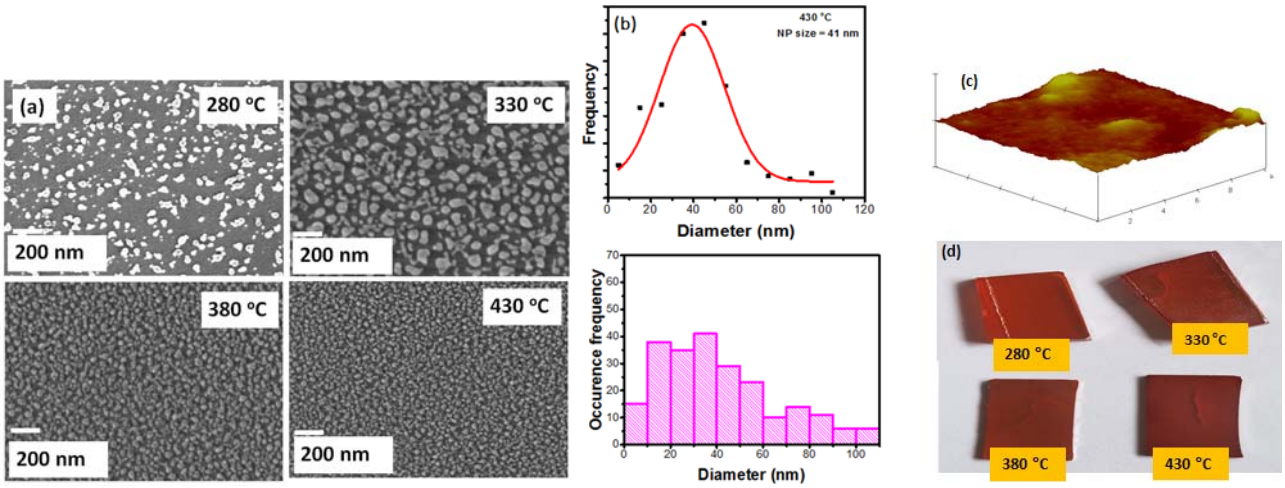

Fig. 5. (a)FE-SEM images of hematite NPs prepared at temperatures of 280°C, 330°C, 380°C and 430°C using chemical spray pyrolysis, concentration 50 mM, and spray pressure of 1.5 $\times 10^5$ Pa, (b) α-Fe_2O_3 NPs distribution using Gaussian fit and histogram, (c) atomic force microscope room mean square (RMS) roughness of hematite NPs at 430°C (d) Images of α-Fe_2O_3 samples as-deposited.

From FE-SEM images in Fig. 5a, the grain size of the hematite samples was decreasing as deposition temperature increased from (280 – 430°C). This is due to the change in structure of α-Fe_2O_3 from amorphous to polycrystalline. At the lowest deposition temperature (280°C), the NPs were amorphous with an average grain size of 100 ± 0.5 nm. As the temperature was increased in steps of 50°C up to 430°C, homogeneous and nanoporous morphology was formed with grain size decreasing to 41 ± 0.5 nm as shown in Fig. 5b. The small and uniform grain structure obtained is suitable for use as a photoanode in the water splitting photoelectrochemical cell. This is due to minimization of the oxygen evolution kinetics largely affected by the short hole diffusion length of hematite (2- 4 nm). Duret et al [37] obtained similar α-Fe_2O_3 NPs using ultrasonic spray pyrolysis, with ferric acetylacetonate as the precursor and ethanol as the solvent. The NPs had a diameter of between 50 and 100 ± 0.5 nm and produced a current density of 1.07μA/cm^2. Fig. 5c shows the atomic force microscope (AFM) topography and surface roughness of hematite films deposited at 430°C. The film possessed an average RMS roughness of 35 nm and homogeneous morphology [20]. Hematite samples synthesized were brown in color, Fig. 5d.

3.4.2 L-arginine/ hematite nanostructures

Hematite films synthesized at a deposition temperature of 430°C were used as seed layer for transformation of NPs to nanospheres using L-arginine biomolecules. This was achieved by CBD at a bath temperature of 90°C for 48 hours. Fig. 6 shows morphology of hematite nanospheres as-obtained by FE-SEM, Gaussian and histogram grain size calculation using imageJ.

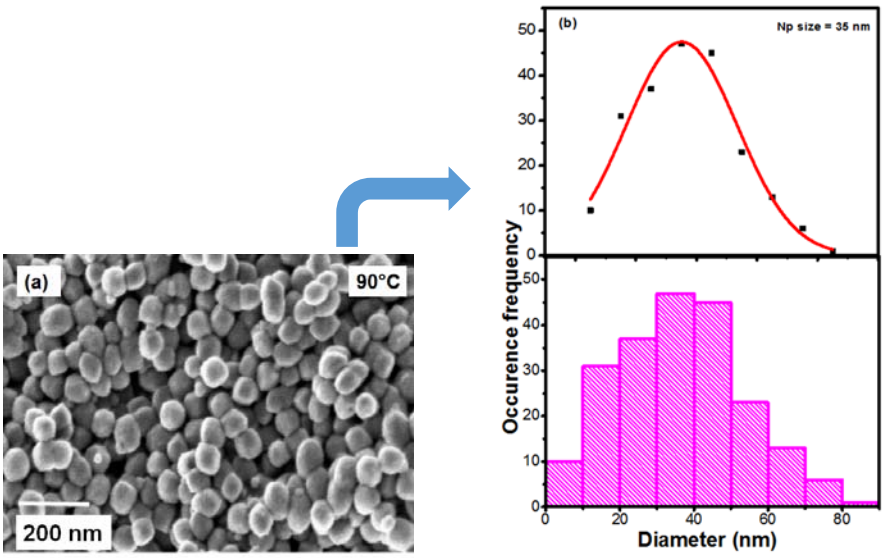

Fig. 6. (a) FE-SEM image of hematite nanospheres using chemical bath deposition at 90°C for 48 hours, (b) Gaussian fit and histogram of the nanosphere size distribution.

From Fig. 6a, the NPs are observed to be spherical and uniform in size, with an average diameter of 30 ± 0.5 nm. The growth of the uniform spherical size and shape was influenced by the functional group of L-arginine (–NH_2 and –COOH) [20]. It was also due to the equi-molar solutions of L-arginine and $FeCl_3.6H_2O$ that were used during transformation process. This led to the uniform interaction of the two solutions and creation of high hydrogen bond between L-arginine and hematite. Iron oxyhydrate which produced uniform transformation of hematite NPs to nanospheres was formed through this interaction process. The formation of iron oxyhydrate can be represented by equation 5 [20], where the second term on the reactant side is the L-arginine molecule, while on the product side, iron oxyhydrate was formed (first term) and the waste product (last term) which was later left to dry and crystallize for further studies.

$$FeCl_3 + C_6H_{14}N_4O_2 + 3H_2O \rightarrow Fe(OH)_3 + 3[H_2NO(NH)NH(CH_2)_3CH(COOH)NH_3^+]Cl^-, \quad (5)$$

Iron oxyhydrate went through the process of heterogeneous nucleation on the seeded layer of hematite NPs forming akagenite (β-FeOOH) phase. β-FeOOH formation was enhanced by the increase of -NH_2 and -COOH functional groups leading to more interaction and transformation. The unstable oxide of iron (akagenite) was then oxidized in air to form α-Fe_2O_3 nanospheres which can be represented in equation 6. The formed α-Fe_2O_3 nanospheres were then nucleated, with uniform distribution on the whole surface of pristine hematite forming uniform nanospheres of equal diameter [20].

$$Fe(OH)_3 \rightarrow \beta - FeOOH \rightarrow \alpha - Fe_2O_3\,, \quad (6)$$

The transformation of hematite NPs to nanospheres can be summarized as shown in Fig. 7.

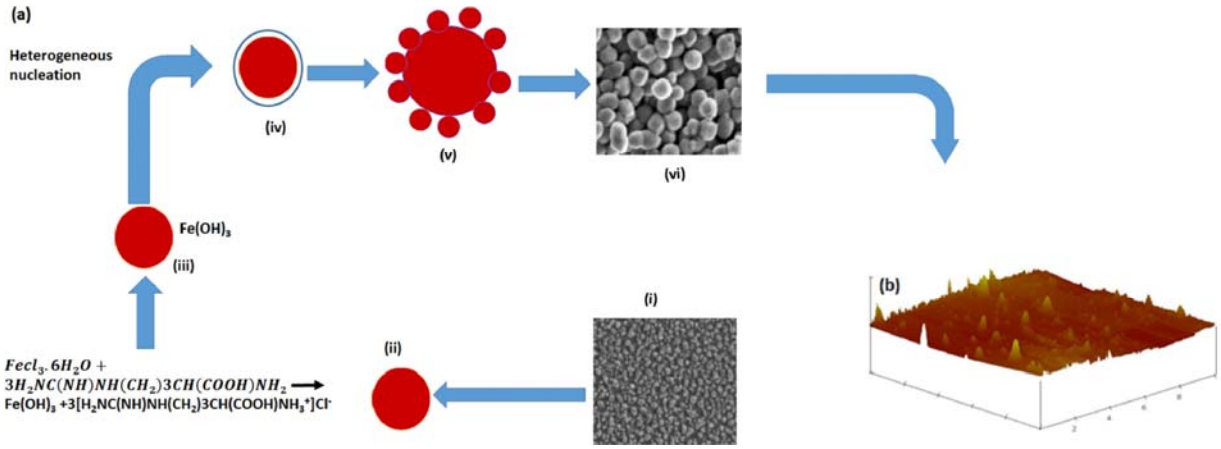

Fig. 7. Heterogeneous nucleation of L-arginine/hematite nanospheres. (i) Hematite NPs prepared by spray pyrolysis, (ii) chemical bath deposition of $FeCl_3.6H_2O$ and L-arginine at a bath temperature of 90°C for 48 hours, (iii) iron oxyhydrate formed that underwent heterogeneous-nucleation in image (iv). The nucleation is uniformly distributed as shown in (v) to form hematite nanospheres, (b) AFM surface RMS roughness of as-prepared L-arginine/hematite nanospheres

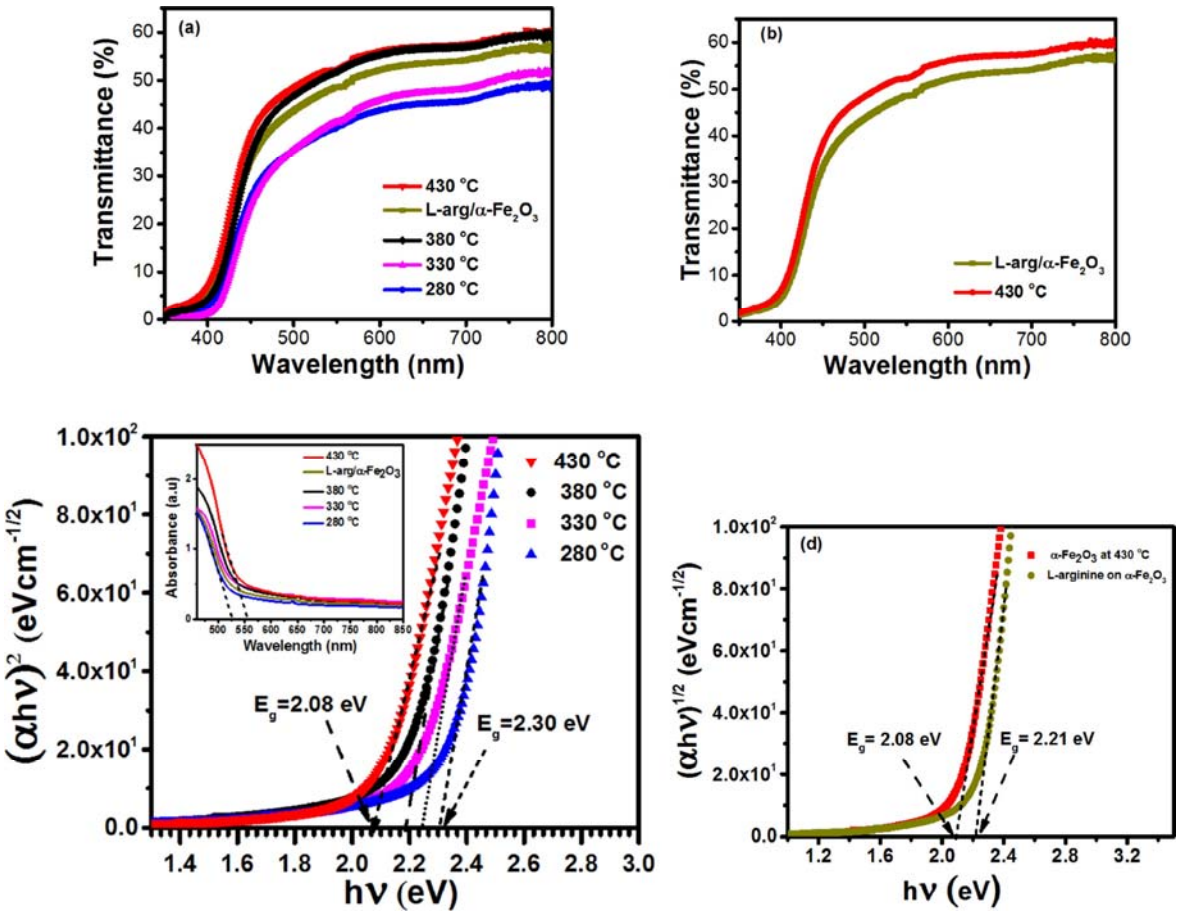

Fig. 8. (a) Transmittance spectra of α-Fe_2O_3 films deposited at temperatures of 280°C, 330°C, 380°C and 430°C using chemical spray pyrolysis, (b) transmittance of α-Fe_2O_3 and L-arginine/hematite nanostructures using chemical bath deposition at a growth temperature of 90°C for 48 hours, (c) variation of $(\alpha h\nu)^2$ versus hν for α-Fe_2O_3 films deposited at different temperatures (280°C, 330°C, 380°C and 430°C), concentration of 50 mM, deposition time of 1 minute and spray pressure of 1.5×10^5 Pa. The inset shows the absorbance of both the α-Fe_2O_3 and L-arginine/hematite nanostructures films (d) $(\alpha h\nu)^2$ versus hν for L-arginine/α-Fe_2O_3 film using chemical bath deposition.

3.5 Optical studies

Optical measurements of hematite NPs were done in the visible region (380 - 800 nm) in order to determine the transmittance, absorbance and energy band gap. Fig. 8a shows the transmittance of α-Fe_2O_3 NPs deposited at different temperatures (280- 430 °C).

A maximum average transmittance of ~47 % was observed in all hematite films at wavelength of 550 nm. The low transmittance recorded was due to several layers of hematite deposited during the synthesis process, which reduced film transparency and increased absorption. As the deposition temperature was increased from 280 to 430°C in steps of 50°C, the maximum transmittance of films was gradually increasing from 44 % (280°C) to 56 % (430°C) at 550 nm in Fig. 8a. This was due to the low film thicknesses obtained at higher temperatures. The obtained results are in agreement with the Lambert-Beer's law ($T=e^{\alpha t}$) [38]. The maximum transmittance for L-arginine/hematite nanostructures in Fig. 8b was observed to decrease slightly from 56 % (α-Fe_2O_3 at 430 °C) to ~49 % at 550 nm due to the slight increase in thickness resulting from L-arginine growth on the seeded hematite layer. Fig. 8c and Fig. 8d shows the $(\alpha h\nu)^2$ against hν of α-Fe_2O_3 nanostructure and L-arginine/ α-Fe_2O_3, where the band gap (E_g) was estimated by extrapolation of linear part with the hν axis. Energy band gap was calculated using Tauc's equation [39],

$$\alpha h\nu = A(h\nu - E_g)^n, \qquad (7)$$

where, α is the absorption coefficient, $h\nu$ is the photon energy, A is a constant, E_g the energy band gap of the semiconductor and n the nature of transition (2 for allowed direct transition and ½ for allowed indirect transition). Hematite films synthesized exhibited an indirect band gap which ranged between 2.30 eV (280°C) and 2.08 eV (430°C) as shown in Fig. 8c. The narrowing of the band gap with increasing deposition temperature was due to the inter-atomic space which widened leading to the reduction of the electron potential. More solar energy is therefore harvested in the visible region by this small band gap of 2.08 eV for α-Fe_2O_3 NPs synthesized at 430°C. The inset in Fig. 8c represents the absorbance versus wavelength of α-Fe_2O_3 at different deposition temperatures (280 - 430°C) and L-arginine/α-Fe_2O_3 NPs synthesized at a constant temperature of 90°C for 48 hours. The onset absorption of hematite NPs ranged between 500 and 560 nm. This absorbance gave the band gap range of 1.90 eV to 2.20 eV using the onset potential calculation, similar to the findings from Bora et al [40]. Fig. 8d shows the band gap of the planar hematite synthesized at 430°C and L-arginine/hematite nanospheres. There was an increase in the band gap from 2.08 eV to 2.21 eV. This was due to the thickness that increased as the transformation process was taking place on the seeded α-Fe_2O_3 layer which further led to change of grain boundary barrier height [41]. Liu et al obtained similar results on nickel doped hematite with a direct band gap of 2.15 eV [42].

4. Conclusion

Hematite NPs were prepared by chemical spray pyrolysis. L-arginine transformed hematite NPs to nanospheres using CBD at a constant temperature of 90°C for 48 hours. FE-SEM results for pristine α-Fe_2O_3 showed uniform grain size of NPs with an average diameter of 41 ± 0.5 nm. The L-arginine transformed NPs with no definite shape to nanospheres with an average grain size of 30 ± 0.5 nm. L-arginine/α-Fe_2O_3 nanospheres showed high surface roughness of 43 nm as opposed to planar α-Fe_2O_3 NPs whose RMS roughness was 35 nm. High surface roughness for hematite films enhances charge transport during PEC water splitting. Raman spectroscopy measurements revealed all seven vibrational phonon modes of α-Fe_2O_3 while XRD results showed rhombohedral polycrystalline nature of hematite, with correct indexing positions of 2θ planes. The thickness of α-Fe_2O_3 nanostructures decreased as the temperature was increased from 280 - 430°C due to high evaporation at higher temperatures, leading to deposition of precursor in vapour form. The films had an average maximum transmittance of ~47 % at 550 nm with the band gap ranging from 2.08 eV to 2.30 eV. The band gap was observed to decrease as the deposition temperature increased gradually. This was due to the increase in inter-atomic spacing, reducing electrode potential. L-arginine/α-Fe_2O_3 nanospheres led to an increase of the band gap from 2.08 eV to 2.21 eV, the latter attributed to the increase in thickness during the growth process. In conclusion, hematite NPs synthesized by both spray pyrolysis and chemical bath deposition have a suitable application as photoanodes for photocurrent production through solar water splitting process. The biomolecule assisted chemical bath deposition can be used to improve the efficiency of hematite in PEC applications by varying the molarity ratio and growth time.

Acknowledgement

The authors wish to thank the Department of Physics, University of Pretoria for the support and provision of all the characterization techniques used in this study and African Laser Centre (ALC) for financial support.

References

[1] Y. Ling, G. Wang, D.A. Wheeler, J.Z. Zhang, Y. Li, Sn-doped hematite nanostructures for photoelectrochemical water splitting, Nano letters, 11 (2011) 2119-2125.

[2] A. Kay, I. Cesar, M. Grätzel, New benchmark for water photooxidation by nanostructured α-Fe_2O_3 films, Journal of the American Chemical Society, 128 (2006) 15714-15721.

[3] B. Eftekharinia, A. Moshaii, A. Dabirian, N.S. Vayghan, Optimization of charge transport in a Co–Pi modified hematite thin film produced by scalable electron beam evaporation for photoelectrochemical water oxidation, Journal of Materials Chemistry A, 5 (2017) 3412-3424.

[4] A. Fujishima, K. Honda, TiO_2 photoelectrochemistry and photocatalysis, Nature, 238 (1972) 37-38.

[5] S.U. Khan, M. Al-Shahry, W.B. Ingler, Efficient photochemical water splitting by a chemically modified n-TiO_2, science, 297 (2002) 2243-2245.

[6] A. Wolcott, W.A. Smith, T.R. Kuykendall, Y. Zhao, J.Z. Zhang, Photoelectrochemical study of nanostructured ZnO thin films for hydrogen generation from water splitting, Advanced Functional Materials, 19 (2009) 1849-1856.

[7] C.-Y. Chiang, K. Aroh, N. Franson, V.R. Satsangi, S. Dass, S. Ehrman, Copper oxide nanoparticle made by flame spray pyrolysis for photoelectrochemical water splitting–Part II. Photoelectrochemical study, International Journal of Hydrogen Energy, 36 (2011) 15519-15526.

[8] A.J. Abel, I. Garcia-Torregrosa, A.M. Patel, B. Opasanont, J.B. Baxter, SILAR-deposited hematite films for photoelectrochemical water splitting: effects of Sn, Ti, thickness, and nanostructuring, The Journal of Physical Chemistry C, 119 (2015) 4454-4465.

[9] Y. Liu, Q. Li, S. Gao, J.K. Shang, Template-free solvothermal synthesis of WO_3/$WO_3 \cdot H_2O$ hollow spheres and their enhanced photocatalytic activity from the mixture phase effect, CrystEngComm, 16 (2014) 7493-7501.

[10] B. Klahr, S. Gimenez, F. Fabregat-Santiago, T. Hamann, J. Bisquert, Water oxidation at hematite photoelectrodes: the role of surface states, Journal of the American Chemical Society, 134 (2012) 4294-4302.

[11] A.A. Yadav, T. Deshmukh, R. Deshmukh, D. Patil, U. Chavan, Electrochemical supercapacitive performance of Hematite α-Fe_2O_3 thin films prepared by spray pyrolysis from non-aqueous medium, Thin Solid Films, 616 (2016) 351-358.

[12] Y.-J. Chen, L.-Y. Chen, Effect of Morphology Control on Hematite Nanostructures for Solar Water Splitting, Energy Procedia, 61 (2014) 2046-2049.

[13] I.S. Cho, H.S. Han, M. Logar, J. Park, X. Zheng, Enhancing Low-Bias Performance of Hematite Photoanodes for Solar Water Splitting by Simultaneous Reduction of Bulk, Interface, and Surface Recombination Pathways, Advanced Energy Materials, 6 (2016) 1501840.

[14] H.-J. Ahn, M.-J. Kwak, J.-S. Lee, K.-Y. Yoon, J.-H. Jang, Nanoporous hematite structures to overcome short diffusion lengths in water splitting, Journal of Materials Chemistry A, 2 (2014) 19999-20003.

[15] D.A. Grave, H. Dotan, Y. Levy, Y. Piekner, B. Scherrer, K.D. Malviya, A. Rothschild, Heteroepitaxial hematite photoanodes as a model system for solar water splitting, Journal of Materials Chemistry A, 4 (2016) 3052-3060.

[16] A.G. Tamirat, J. Rick, A.A. Dubale, W.-N. Su, B.-J. Hwang, Using hematite for photoelectrochemical water splitting: a review of current progress and challenges, Nanoscale Horizons, 1 (2016) 243-267.

[17] Q. Peng, J. Wang, Z. Feng, C. Du, Y. Wen, B. Shan, R. Chen, Enhanced photoelectrochemical water oxidation by fabrication of p-$LaFeO_3$/n-Fe_2O_3 heterojunction on hematite nanorods, The Journal of Physical Chemistry C, 121 (2017) 12991-12998.

[18] Y. Lin, S. Zhou, S.W. Sheehan, D. Wang, Nanonet-based hematite heteronanostructures for efficient solar water splitting, Journal of the American Chemical Society, 133 (2011) 2398-2401.

[19] Z. Pu, M. Cao, J. Yang, K. Huang, C. Hu, Controlled synthesis and growth mechanism of hematite nanorhombohedra, nanorods and nanocubes, Nanotechnology, 17 (2006) 799.

[20] H. Cao, G. Wang, J.H. Warner, A.A. Watt, Amino-acid-assisted synthesis and size-dependent magnetic behaviors of hematite nanocubes, Applied Physics Letters, 92 (2008) 013110.

[21] J.A. Navío, G. Colón, M. Macías, C. Real, M.I. Litter, Iron-doped titania semiconductor powders prepared by a sol–gel method. Part I: synthesis and characterization, Applied Catalysis A: General, 177 (1999) 111-120.

[22] M. Mohapatra, S. Anand, Synthesis and applications of nano-structured iron oxides/hydroxides–a review, International Journal of Engineering, Science and Technology, 2 (2010).

[23] C.I. Sun, H.H. Soo, L. Manca, P. Joonsuk, Z. Xiaolin, Enhancing Low-Bias Performance of Hematite Photoanodes for Solar Water Splitting by Simultaneous Reduction of Bulk, Interface, and Surface Recombination Pathways, Advanced Energy Materials, 6 (2016) 1501840.

[24] X. Hu, J.C. Yu, J. Gong, Q. Li, G. Li, α-Fe_2O_3 nanorings prepared by a microwave-assisted hydrothermal process and their sensing properties, Advanced Materials, 19 (2007) 2324-2329.

[25] Y. Hu, D.K. Bora, F. Boudoire, F. Häussler, M. Graetzel, E.C. Constable, A. Braun, A dip coating process for large area silicon-doped high performance hematite photoanodes, Journal of Renewable and Sustainable Energy, 5 (2013) 043109.
[26] F.L. Souza, K.P. Lopes, P.A. Nascente, E.R. Leite, Nanostructured hematite thin films produced by spin-coating deposition solution: Application in water splitting, Solar energy materials and solar cells, 93 (2009) 362-368.
[27] A. Lassoued, B. Dkhil, A. Gadri, S. Ammar, Control of the shape and size of iron oxide (α-Fe_2O_3) nanoparticles synthesized through the chemical precipitation method, Results in physics, 7 (2017) 3007-3015.
[28] K.H. Abass, Fe_2O_3 thin films prepared by spray pyrolysis technique and study the annealing on its optical properties, International Letters of Chemistry, Physics and Astronomy, 6 (2015) 24-31.
[29] D. Perednis, L.J. Gauckler, Thin film deposition using spray pyrolysis, Journal of electroceramics, 14 (2005) 103-111.
[30] R. Morrish, M. Rahman, J.D. MacElroy, C.A. Wolden, Activation of hematite nanorod arrays for photoelectrochemical water splitting, ChemSusChem, 4 (2011) 474-479.
[31] A.A. Yadav, Preparation and electrochemical properties of spray deposited α-Fe_2O_3 from nonaqueous medium for supercapacitor applications, Journal of Materials Science: Materials in Electronics, 27 (2016) 12876-12883.
[32] J. Hua, J. Gengsheng, Hydrothermal synthesis and characterization of monodisperse α-Fe_2O_3 nanoparticles, Materials Letters, 63 (2009) 2725-2727.
[33] T. Mariño-Otero, M. Oliver-Tolentino, M.A. Aguilar-Frutis, G. Contreras-Martínez, E. Pérez-Cappe, E. Reguera, Effect of thickness in hematite films produced by spray pyrolysis towards water photo-oxidation in neutral media, international journal of hydrogen energy, 40 (2015) 5831-5836.
[34] J. Morales, J. Tirado, M. Macias, Changes in crystallite size and microstrains of hematite derived from the thermal decomposition of synthetic akaganéite, Journal of Solid State Chemistry, 53 (1984) 303-312.
[35] S. Xie, E. Iglesia, A.T. Bell, Effects of temperature on the Raman spectra and dispersed oxides, The Journal of Physical Chemistry B, 105 (2001) 5144-5152.
[36] G. Lucazeau, Effect of pressure and temperature on Raman spectra of solids: anharmonicity, Journal of Raman Spectroscopy, 34 (2003) 478-496.
[37] A. Duret, M. Grätzel, Visible light-induced water oxidation on mesoscopic α-Fe_2O_3 films made by ultrasonic spray pyrolysis, The Journal of Physical Chemistry B, 109 (2005) 17184-17191.
[38] A.S. Hassanien, A.A. Akl, Optical characteristics of iron oxide thin films prepared by spray pyrolysis technique at different substrate temperatures, Applied Physics A, 124 (2018) 752.
[39] J. Gao, Q. Zhao, Y. Sun, G. Li, J. Zhang, D. Yu, A novel way for synthesizing phosphorus-doped ZnO nanowires, Nanoscale Research Letters, 6 (2011) 45.
[40] D.K. Bora, Hematite and its hybrid nanostructures for photoelectrochemical water splitting: how do properties affect functionality?, University_of_Basel, 2012.
[41] A. Kumar, K. Yadav, Optical properties of nanocrystallite films of α-Fe_2O_3 and α-$Fe_{2-x}Cr_xO3$ ($0.0 \leqslant x \leqslant 0.9$) deposited on glass substrates, Materials Research Express, 4 (2017) 075003.
[42] Y. Liu, Y.-X. Yu, W.-D. Zhang, Photoelectrochemical properties of Ni-doped Fe_2O_3 thin films prepared by electrodeposition, Electrochimica Acta, 59 (2012) 121-127.